Research Article

Effect of the Interaction between Cavities and Flaws on Rock Mechanical Properties under Uniaxial Compression

Jianwang Li,[1,2] **Yu Zhou** [ID],[1] **Wei Sun,**[1] **and Zheng Sun**[1]

[1]*Key Laboratory of Ministry of Education for Efficient Mining and Safety of Metal Mine,*
 University of Science and Technology Beijing, Beijing 100083, China
[2]*China Railway 16th Bureau Group Co., Ltd., Beijing 100018, China*

Correspondence should be addressed to Yu Zhou; westboy85@ustb.edu.cn

Cavities and flaws are common types of defects in rock specimens that have an important impact on the mechanical properties of rockmass. In this paper, cement mortar was used to prefabricate a rock-like specimen with two cavities and a single flaw, and the uniaxial compression test was carried out. The process of fracture evolution on the specimen surface was obtained by using photography technology. The evolution regularity of a fracture was monitored by utilizing acoustic emission (AE) technology during the process of the specimen failure. Moreover, three-dimensional (3D) tomograms of specimens after uniaxial compression were obtained by using computerized tomography (CT) scanning technology, investigating the development characteristics of microcracks and the distribution of the final macrofractures. The particle flow code in two dimensions (PFC2D) program was used to simulate the mechanical behavior of brittle rock combining with microcrack propagation. The calculated stress-strain curve, AE features, and fracture distribution of the specimen obtained from the PFC2D simulation were relatively consistent with the experimental results.

1. Introduction

As the main medium for an engineering construction such as a tunnel, slope, and foundation, the bearing capacity of rockmass directly affects the stability of the projects. In long-term geological processes, many macroscopic and microscopic defects such as cavities, flaws, and joints have been developed in rock materials. However, the mechanical properties of rocks are closely related to the shape, size, and spatial distribution of the internal defects [1, 2]. Therefore, the crack evolution mechanism of rock containing defects has long been one of the focuses of rock mechanics.

In recent years, many scholars have conducted extensive laboratory research on the strength and deformation characteristics of rock with defects and fracture evolution. Wong and Einstein adopted the method of high-speed photography and electron microscopy to study the macroscopic mechanisms and laws of fracture initiation, propagation, and connection in fractured gypsum and marble under uniaxial compression [3, 4]. Yang et al. analyzed the influence of the rock bridge dip angle on the strength in sandstone containing three prefabricated flaws and discussed the fracture propagation mechanism under uniaxial compression [5, 6]. Prudencio et al. also performed a similar study on the compressive mechanical properties of flawed rockmass [7, 8]. In addition, AE monitoring [9–13] technology and CT [14, 15] scanning technology have also been widely used in the experimental research on the macroscopic and microscopic mechanical properties and fracture mechanism of rock with defects. However, there are still some deficiencies in the current research methods for rock fracture. For example, high-speed photography can only capture the fracture characteristics of the specimen surface; an AE monitoring sensor is mounted on the rock surface at a shallow depth, and noise interference is serious, so the results of the analysis rely mainly on the experience of the engineers. Therefore, most of the experimental techniques lack accurate acquisition of the internal fracture space

information during the process of rock failure. However, CT scanning relies on its 3D X-ray tomography imaging technology to achieve high-precision comprehensive observation both inside and outside the rock, so it can make up shortcomings of other methods well.

In recent years, with the substantial increase in computer performance, the PFC program based on particle flow theory has been widely used in various types of rock mechanics and engineering simulations [16–23]. As the PFC program uses the particles to build a calculation model, the bond between the particles will be damaged by the external force and produce microcracks to simulate the break-up and evolution process in the model. Therefore, PFC is very suitable for the study of rock fracture mechanisms and has become a new research method. At present, when using the PFC program to simulate rock mechanics behavior, the traditional bonded-particle model (BPM) [24], grain-based model (GBM) [25], and flat-joint model (FJM) [26] are usually included. In BPM, the calculation model consists of round particles with the advantages of a simple model and high computational efficiency. However, due to the use of circular particles to construct the model, there is no self-locking effect between the particles, and the characteristics of the ratio between tensile and uniaxial strength of rock cannot be reproduced. To solve the defects of the BPM, the GBM and FJM were developed by Potyondy. The GBM and FJM can build irregular mineral particles that reproduce the self-locking effect between particles. The GBM can also simulate the transgranular breakdown of mineral particles. Therefore, the GBM and FJM are very suitable for simulating brittle rocks. However, due to the increase in the number of particles and irregular contact boundaries, the GBM and FJM have the disadvantage of low computational efficiency. In other discrete element methods, some scholars such as Misra and Singh [27] and Poorsolhjouy and Misra [28] have also used the idea of building computational models by irregular particles to simulate the mechanical behavior of rock materials.

At present, the research on the mechanical properties of rock with defects focuses mainly on the interaction mechanism of single morphological defects such as cavities and flaws. However, there is a lack of in-depth research on the interaction mechanism between different defects such as cavities and flaws in the rock. In this paper, we intend to use AE technology, photography technology, and CT scanning technology synthetically, combined with particle flow theory and the PFC program, to study the effect of the interaction between cavity and flaw on the rock mechanical properties under uniaxial compression.

2. Research Method

2.1. Specimen Preparation.
To research the crack evolution during the interaction of cavity and flaw in rockmass, cement mortar was used to prepare specimens. The cement mortar consisted of cement, sand, and water in the ratio of 1 : 2 : 0.6. The cement mortar utilized R42.5 cement, and the sand consisted of natural fine river sand with a particle size of less than 1.5 mm. The specimen was a rectangular parallelepiped with a size of 50 mm × 50 mm × 100 mm.

One flaw and two cavities were prefabricated in the rock specimen, perpendicular to the specimen surface, and running through the surface. The length of the flaw was 10 mm, and the width was 0.4 mm; the angle between the flaw and the loading direction was 45°, and the midpoint of the flaw was in the geometric center of the specimen. The diameter of the two cavities was 10 mm, and both of the cavities were symmetrically arranged along the center of the specimen. The distance between the cavity center and the loading end was 30 mm, while the distance between the cavity center and the lateral surface was 15 mm. The geometrical morphology of the flaw and cavity is shown in Figure 1(a). The poured cement mortar specimen was cured at room temperature for 24 hours and then striped. The specimen was then kept in a curing box with constant temperature (19.9°C) and constant humidity (97%) for 28 days.

2.2. Experimental Process.
The experimental system consists of the loading system, the observation system, and the AE monitoring system, which are shown in Figure 1(b).

A YAW-600 electro hydraulic servo rock testing machine was used as the loading system. To reduce the impact of boundary friction, Vaseline was applied to the upper and lower surfaces of the test specimen, and the loading board was padded before loading. Displacement control was used as the load mode with a loading rate of 0.002 mm/s. The test was stopped when the specimen residual strength was 20% of the peak strength. An HDR-CX405 HD digital video camera produced by Sony Corporation was used as the observation system, shooting the process of fracture evolution on the specimen surface. The spatial evolution model of microcrack generation and expansion inside the specimen was monitored by utilizing AE technology during the experiment. AE is a common phenomenon reflecting brittle failure within rock-like materials (including the generation and expansion of microcracks). The AE monitoring system used in experiment was IMaGE AE monitoring system manufactured by America Itasca Company. The raw signal was stored in two data collection mainframes (master and slave) and processed by a trigger method. The corresponding AE setup parameters were as follows: amplifier gain 50 dB, pretrigger 100 samples, threshold level 0.1 V, sampling frequency 5 MHz, and dead time 1024 samples (2.048×10^{-4} s).

The NanoVoxel-3502E scanning system produced by China Tianjin Sanying Company was used for CT scanning of the broken specimen to learn the distribution regularity of the fracture in the specimen. The maximum spatial resolution for this CT scanning system is $0.5\,\mu$m. Multiscale internal information of fracture in rock can be detected without destruction. Therefore, CT scanning technique was widely used in investigating the rock fracture development characteristics, rock cavity structure, etc. The CT system consists of a ray source, detector, mechanical system, computer system, and antiradiation box, as shown in Figure 2. The light provided by the ray source satisfies the test requirements. The detector ensures the collection of frames and image quality. The mechanical system should meet the
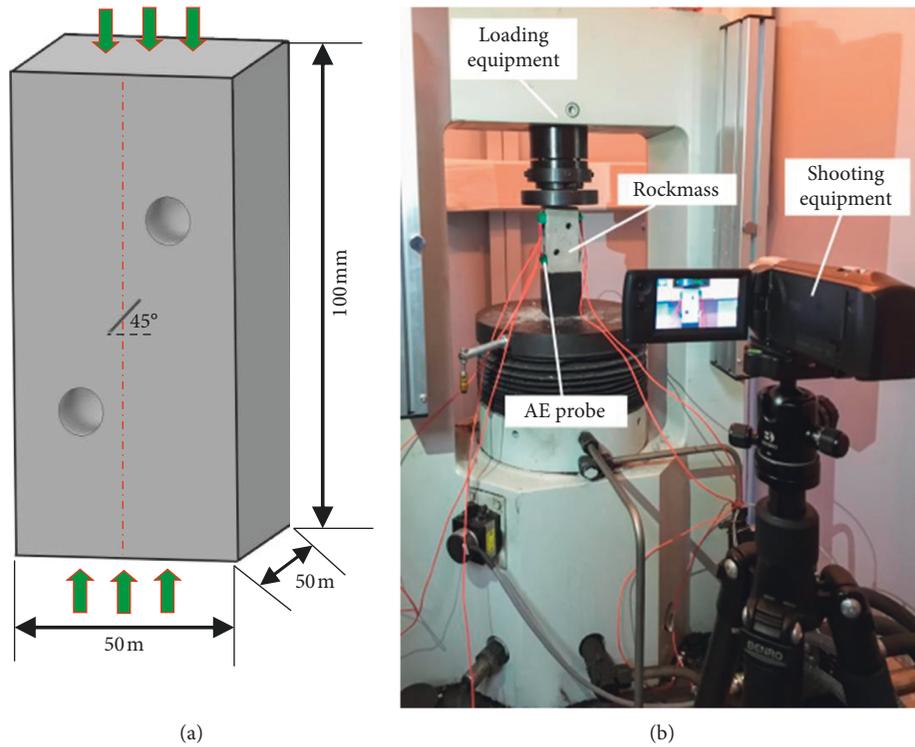
(a)

(b)

Figure 1: Experimental specimen and system: (a) geometric form of specimen; (b) layout of the test system.
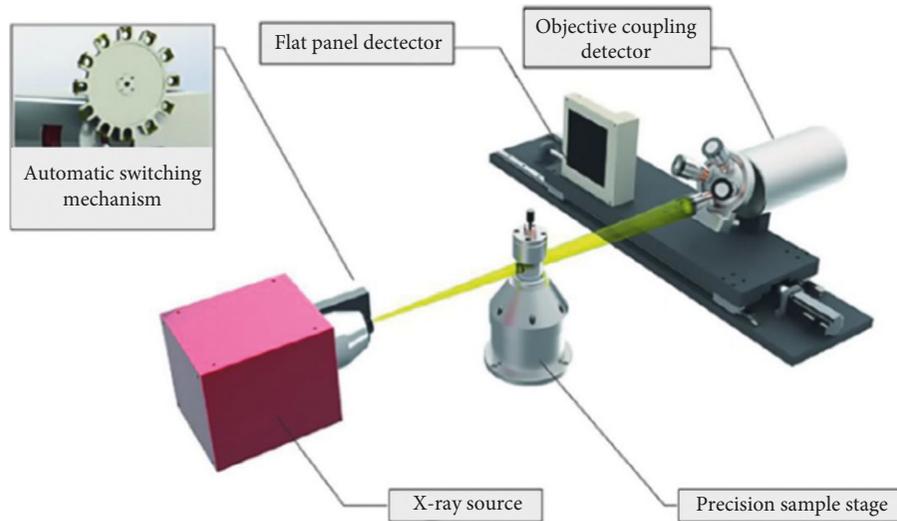

Figure 2: Imaging principle of X-ray.

precision test requirement of high-resolution reconstruction. The computer system is utilized to control the mechanical system, ensuring data collection and reconstruction analysis well. The radiation is shielded by the antiradiation box to guarantee the safety of the tester.

2.3. Simulation Method. As a discrete element numerical method with a high development in recent years, particle flow theory and the PFC program can determine the mechanical properties of rock, concrete, and other geotechnical

materials by solving the interaction and movement between circular or spherical particles [29]. In the PFC program, a bond model is used to represent rock-type materials by bonding the particles together, and the traditional bond model is BMP [24]. In the PFC2D and PFC3D programs, disks and spheres, which are rigid materials with a friction coefficient and normal and tangential stiffness, are used to represent particles. There are two kinds of particle bond models, namely, the contact bond model and the parallel bond model [30], and they both have an elastic, brittle body. The sample in this paper is a precast rock-like sample with

low brittleness and a self-locking effect. Balancing the computational efficiency and the accuracy of the simulation, we decided to use BPM for simulation.

In this paper, the reasonable microscopic parameters were selected using the uniaxial compression test of an intact sample. The size of the calculation model established was consistent with the test specimen, and the parallel bond model was selected as the bond model. The calculated loading rate was set to be small enough to ensure the quasi-static loading state, and the axial loading rate was set to 1.0. When the residual strength of the specimen reached 20% of the peak intensity, the calculation was terminated. Through repeated debugging, the final calculation micromechanical parameters are shown in Table 1.

3. Analysis of the Experimental and Calculation Results

3.1. Effect of the Cavities and Flaw on AE Properties. The stress-strain curve and AE events obtained from the test are shown in Figure 3(a). The stress-strain curve and the number of microcracks obtained from the calculation are shown in Figure 3(b). From the experimental stress-strain curve, the peak strength is approximately 15.5 MPa with the strain of 2.7×10^{-3}, and the elastic modulus before the peak strength is approximately 5.7 GPa. From the calculated stress-strain curve, the peak strength is approximately 15.4 MPa, with the strain of 2.7×10^{-3}, and the elastic modulus before the peak strength is also approximately 5.7 GPa. The experimental stress-strain curve shows a concave upward trend before the strain reaches 0.8×10^{-3} in the prepeak stage, and this is the stage of the original tiny void compaction in the specimen. Until reaching the peak strength, the experimental stress-strain curve shows an approximately linear upward trend with a small stress drop in the middle of the stage. After the peak strength, the experimental stress-strain curve shows the step-and-shock signal decreases, accompanied by two large stress drops. In the calculation results, the stress-strain curve shows an approximately linear upward trend before the prepeak stage from the beginning of loading because the particles constructed in the model are in close contact with each other, and there is no particle with a contact number less than three. After the peak strength, the calculated stress-strain curve shows a step decrease, accompanied by two large stress drops. One stress drop is relatively subdued, and the other is more intense.

There are a total of 2413 AE events monitored from the AE experiment. Among these AE events, 665 are prepeak events, accounting for approximately 27.6%. There are a total of 1748 postpeak events, accounting for approximately 72.4%. In the prepeak region, there are relatively few AE events before the strain reaches 1.6×10^{-3} (minor stress drop before the peak strength), with 168 AE events, accounting for 7.0% of the total. After the minor stress drop before the peak strength, AE events become active until the moment of the peak strength, with 497 AE events accounting for 20.6% of the total. After the peak strength, AE events become more active. In general, when the calculated stress-strain curve drops under stress, the number of AE events increases sharply. The greater the absolute value of stiffness under the stress drop is, the greater the AE event rate is. For example, at the only time stress drops before the peak strength (the strain changes from 1.55×10^{-3} to 1.63×10^{-3}), the absolute value of stiffness is 15.76 GPa, and the number of AE events generated is 168 (the number of corresponding AE event rate is 21 per 10^{-5} strain). After the peak strength, at the first stress drop with the strain changing from 2.70×10^{-3} to 2.83×10^{-3}, the absolute value of stiffness is 15.38 GPa, and the number of AE events generated is 152 (the number of corresponding AE event rate is 12 per 10^{-5} strain). At the second stress drop with the strain changing from 2.99×10^{-3} to 3.30×10^{-3}, the absolute value of stiffness is 16.17 GPa, and the number of AE events generated is 162 (the number of corresponding AE event rate is 5 per 10^{-5} strain). At the third stress drop with the strain changing from 4.37×10^{-3} to 4.50×10^{-3}, the absolute value of stiffness is 30.77 GPa and the number of AE events generated is 469 (the number of corresponding AE event rate is 36 per 10^{-5} strain).

The microcracks generated in the calculation can be divided into microtensile and shear cracks. The microcracks are generated because the stress between the particles exceeds the bond strength. A total of 1247 microcracks are obtained from the calculation. There are 271 microcracks before the peak strength, accounting for approximately 21.7%, while there are 976 microcracks after the peak strength, accounting for approximately 78.3%. When the strain equals 1.9×10^{-3} and the stress equals 11.2 MPa, microcracks begin to appear inside the specimen. Then, there is a rapid increase in the microcrack event rate. After the peak strength, the generation of the microcracks becomes more active. At the stress drop stage, the larger the absolute value of stiffness is, the larger the microcrack event rate is. For example, after the peak strength, at the first stress drop with the strain changing from 2.75×10^{-3} to 3.52×10^{-3}, the absolute value of stiffness is 10.00 GPa, and the number of microcracks generated is 641 (the number of corresponding microcrack event rate is 3 per 10^{-4} strain). At the second stress drop with the strain changing from 3.60×10^{-3} to 3.74×10^{-3}, the absolute value of stiffness is 36.07 GPa, and the number of microcrack generated is 469 (the number of corresponding microcrack event rate is 335 per 10^{-4} strain).

In general, the stress-strain curve and AE characteristics obtained from the experiment are consistent with the calculation. Comparing the test with the calculated results, the number of AE events after the strength peak of the sample has an advantageous position. At the beginning of loading, the number of AE events is small. As the load continues, the number of AE events increase. After the strength peak, the AE events begin to explode on a large scale. The greater the stress drop is, the greater the number of AE events is, and the higher the degree of sample damage is.

3.2. Effect of the Cavities and Flaw on the Generation of Fractures. The process of the fracture evolution is shown in Figure 4, and its corresponding stress-strain state is shown in Figure 3(a). The macrofractures generated during the

TABLE 1: Mesomechanical parameters of the calculation model.

Name (unit)	Minimum particle radius, R_{min} (mm)	Maximum-minimum particle radius ratio, R_{rat}	Particle volume density, ρ (kg·m^{-3})	Interparticle friction coefficient, μ	Particle elastic modulus E_c, (GPa)	Particle normal-tangential stiffness ratio, k_n/k_s	—
Value	0.25	1.66	2100	1	4.70	2.0	—

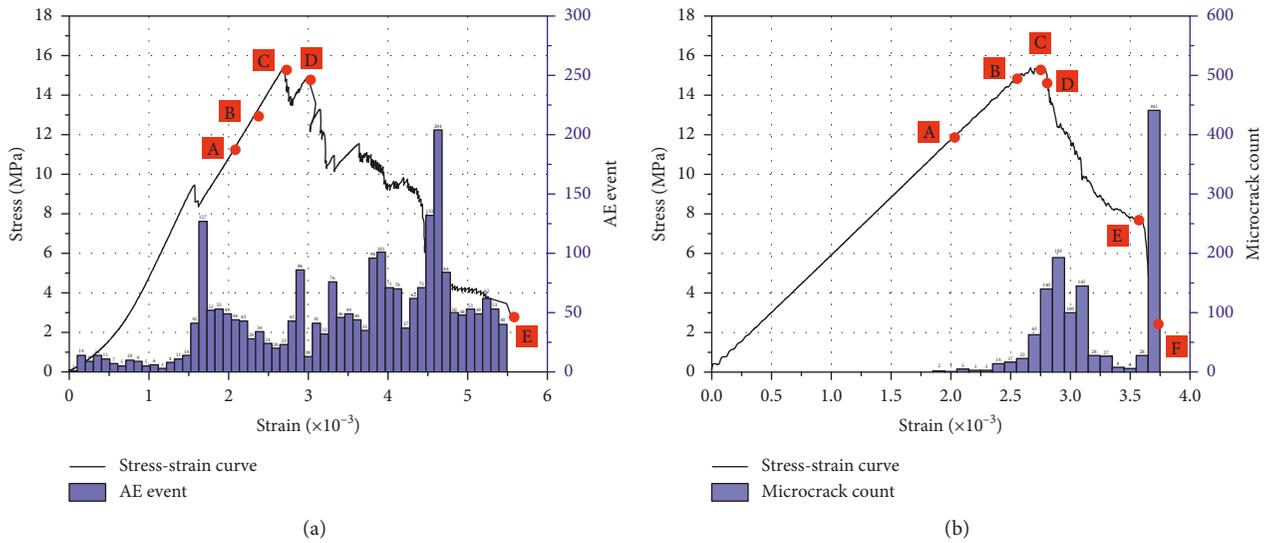| Name (unit)	Coefficient of parallel viscosity, λ	Parallel bond elastic modulus, $\bar{E}_c$ (GPa)	Parallel bond normal-tangential stiffness ratio, $\bar{k}_n/\bar{k}_s$	Average\normal bond strength, $\sigma_{n\text{-mean}}$ (MPa)	Standard deviation of the normal bond strength, $\sigma_{n\text{-dev}}$ (MPa)	Average shear bond strength, $\tau_{s\text{-mean}}$ (MPa)	Standard deviation of the shear bond strength, $\tau_{s\text{-dev}}$ (MPa)
Value	1	4.70	2.0	20.0	2.0	20.0	2.0

FIGURE 3: Stress-strain curves and AE properties: (a) stress-strain curve and AE events obtained from experiment; (b) stress-strain curve and cracks obtained from calculation.
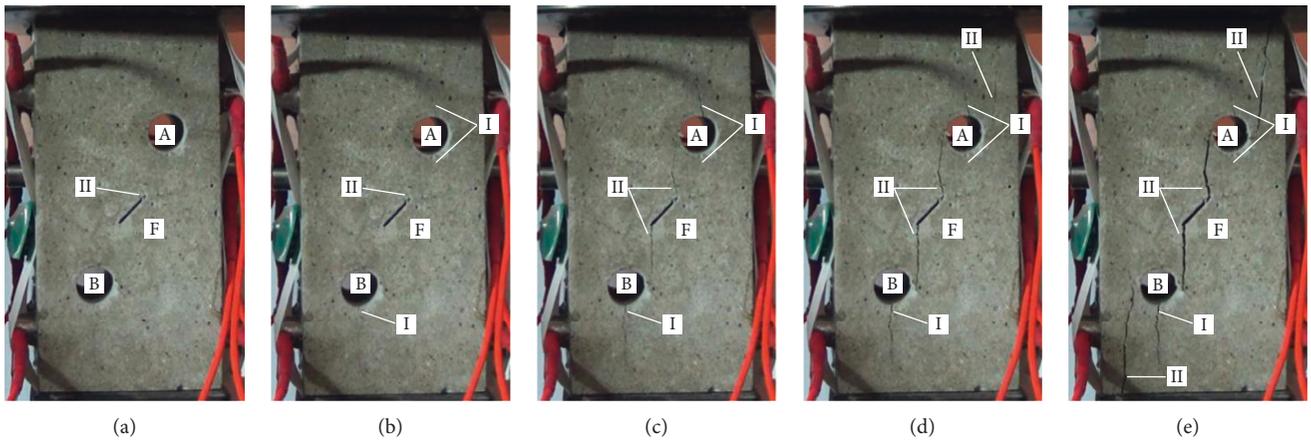

FIGURE 4: The evolution process of the fracture obtained from the experiment: (a) $\varepsilon = 2.06 \times 10^{-3}$, $\sigma = 11.21$ MPa; (b) $\varepsilon = 2.30 \times 10^{-3}$, $\sigma = 12.82$ MPa; (c) $\varepsilon = 2.71 \times 10^{-3}$, $\sigma = 15.47$ MPa; (d) $\varepsilon = 3.06 \times 10^{-3}$, $\sigma = 12.78$ MPa; (e) $\varepsilon = 5.54 \times 10^{-3}$, $\sigma = 2.90$ MPa.

specimen failure can be divided into two types. One is the type-I fracture (also called wing tensile fracture), and its width is usually relatively thin, developing along the loading direction. The other is the type-II fracture (also called shear fracture), and its width is usually relatively wide, developing along the direction with a certain angle to the loading. Before the peak strength, when the strain equals 2.06×10^{-3} and the stress equals 11.21 MPa, the macroscopic fractures appear

at the end of the flaw at first. At the top of the flaw F, type-II fractures are generated at this time. When the strain equals 2.30×10^{-3} and the stress equals 12.82 MPa, type-I fractures begin to generate at the top and bottom of the cavity A and B. When the stress reaches the peak strength (the strain is equal to 2.71×10^{-3} and the stress is equal to 15.47 MPa), type-II fractures between the top of the flaw F and the cavity A and between the bottom of flaw F and the cavity B run through completely. At the same time, the type-I fractures at the top and bottom of the cavities A and B develop sequentially. After the peak strength, when the strain equals 3.06×10^{-3} and the stress equals 12.78 MPa, there is a significant stress drop and type-II fractures appear at the right side of cavity A. When the strain equals 5.54×10^{-3} and the stress equals 2.90 MPa, there are two significant stress drops before the end of the experiment. At this moment, type-II fractures at the right side of cavity A develop sequentially, while type-II fractures are also generated at the left side of cavity B.

The evolution process of microcracks obtained from the calculation is shown in Figure 5, and its corresponding state of stress-strain has been marked in Figure 3(b). In the figure, the tensile microcrack is represented by the short red line and the shear microcrack is represented by the short blue line. Before the peak strength, when the strain equals 2.03×10^{-3} and the stress equals 11.8 MPa, microcracks are generated at both ends of flaw F first and then develop sequentially, forming the later type-I macrofractures. When the strain equals 2.59×10^{-3} and the stress equals 15.0 MPa, the microcracks that form type-II fractures also begin to appear at both ends of flaw F, and the microcracks that form type-I fractures begin to appear at the top and bottom of the cavity A and B. At the same time, a few microcracks begin to generate at the right side of cavity B, but they do not extend widely before the peak strength. When the stress reaches the peak strength (the strain is equal to 2.73×10^{-3} and the stress is equal to 15.4 MPa), type-II fractures between the top of the flaw F and the cavity A run through completely, and type-I fractures continue to expand at the bottom of flaw F, while the type-I fractures expand farther at the top and bottom of the cavities A and B. After the peak strength, when the strain equals 2.81×10^{-3} and the stress equals 14.5 MPa, the type-II fractures between flaw F and cavity B also run through completely. When the strain equals 3.59×10^{-3} and the stress equals 7.8 MPa, a stress drop with a relatively long duration and large amplitude occurs, and the type-II fractures between the left side of cavity B and the boundary of the specimen run through completely. When the strain equals 3.73×10^{-3} and the stress equals 2.5 MPa, the type-II fractures between the right side of cavity A and the boundary of the specimen also run through completely. There are also a few type-I cracks evolving from the extension of the type-II fractures at the outside of the cavity after the peak strength.

3.3. Effect of the Cavities and Flaw on the Distribution of Fractures. Based on the comparative analysis of the

experimental and calculated results, the evolution regularity and distribution type of macrofractures are relatively consistent during the specimen failure. The regularities can be summarized as follows: (1) before the peak strength, the fractures first generate at the two ends of the flaw, then the type-I fractures begin to appear at the top and bottom of the cavity; (2) at the moment of the peak strength, the type-II fractures between the ends of the flaw and the side wall of the cavity almost run through completely; and (3) after the peak strength, the type-II fractures between the outside of the cavity and the boundary of the specimen begin to expand and gradually run through, with a relatively obvious stress drop correspondingly.

The fracture distribution information after the experiment, which was obtained by using CT scanning technology, is shown in Figure 6. Along the trend direction of the prefabricated flaws, a scanning section was set at 12.5 mm. There are five scanning sections, as follows: $M_1N_1P_1Q_1$, $M_2N_2P_2Q_2$, $M_3N_3P_3Q_3$, $M_4N_4P_4Q_4$, and $M_5N_5P_5Q_5$. Compared with the fracture distribution information obtained from the photography technology, the fracture distribution information of the surface and internal to the specimen obtained from CT scanning technology is clearer. Especially for the type-I fracture, it is not easily captured with photography technology. Along the trend direction of the prefabricated flaws, the distribution of fractures in the five scanning sections is almost unanimous. The type-II fractures run through at the rock bridge between the flaw and the cavity, while the type-I fractures develop along the loading direction at the flaw ends. The type-I fractures generated at the top and bottom of the cavity develop along the loading direction, while in the process of the type-II fractures generating at the outside of the cavity, there are a few type-I fractures generated from them at the same time. In the width of the fracture, the type-I fractures are significantly different from the type-II fractures. For example, on the $M_1N_1P_1Q_1$ section, the widths of the type-I fracture and type-II fracture generated at the ends of flaw F are 0.27 mm and 0.55 mm, respectively. On the $M_4N_4P_4Q_4$ section, the widths of the type-I fracture and type-II fracture generating at the left side of cavity B are 0.19 mm and 0.36 mm, respectively. The width of the type-II fracture is always wider and approximately two times wider than the width of the type-I fracture. In general, the fracture distribution information inside the specimen obtained from CT scanning technology at the end of the experiment is approximately consistent with the information obtained from the PFC calculation, indicating that the calculation results are reliable.

4. Conclusions

(1) During the process of the specimen failure, AE events appear mainly after the peak strength. The larger the absolute value of stiffness during the stress drop is, the larger the AE event rate is. A larger stress drop generally corresponds to the generation of a shear fracture.

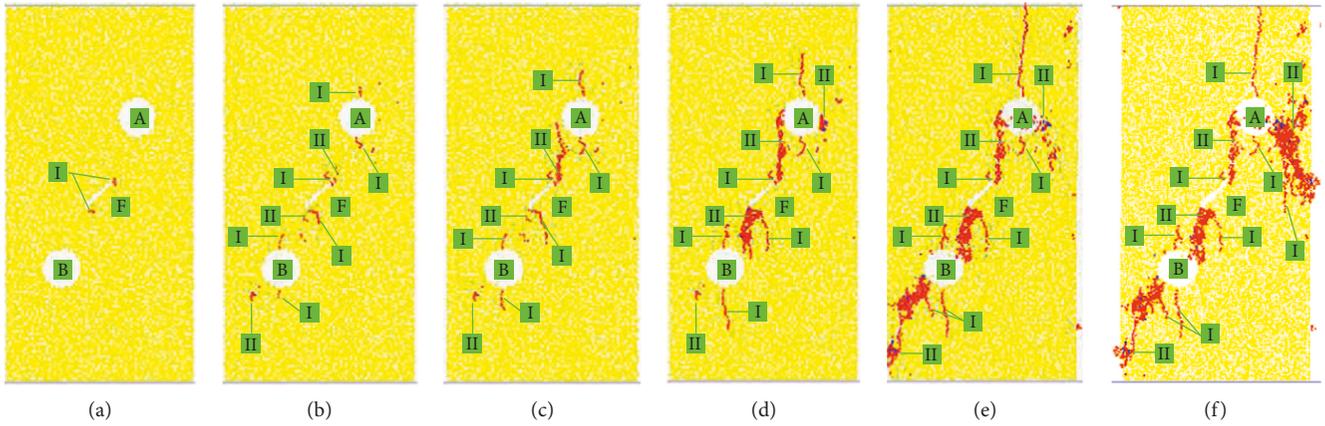(2) Fractures can be divided into two categories, namely, wing tensile fracture (type-I fracture) and shear

FIGURE 5: The evolution process of the microcracks obtained from the calculation: (a) $\varepsilon = 2.03 \times 10^{-3}$, $\sigma = 11.8$ MPa; (b) $\varepsilon = 2.59 \times 10^{-3}$, $\sigma = 15.0$ MPa; (c) $\varepsilon = 2.73 \times 10^{-3}$, $\sigma = 15.4$ MPa; (d) $\varepsilon = 2.81 \times 10^{-3}$, $\sigma = 14.5$ MPa; (e) $\varepsilon = 3.59 \times 10^{-3}$, $\sigma = 7.8$ MPa; (f) $\varepsilon = 3.73 \times 10^{-3}$, $\sigma = 2.5$ MPa.
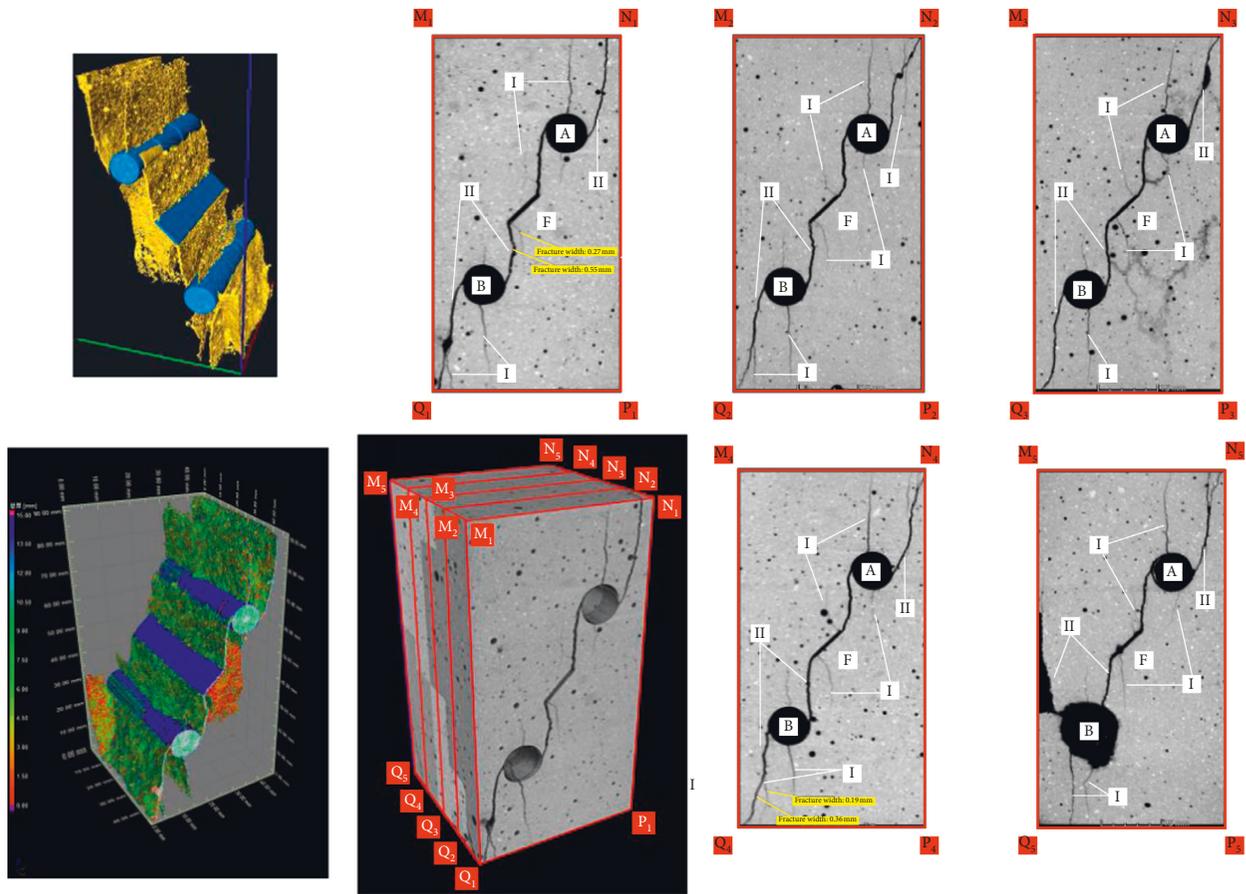

FIGURE 6: The fracture distribution information inside the specimen obtained by CT scanning.

fracture (type-II fracture). The type-I fractures generate mainly at the ends of the flaw or at the top and bottom of the cavity, developing along the loading direction. The type-II fractures generate mainly between the flaw and the cavity and between the cavity and the boundary of the specimen, developing along the direction with a certain angle to the loading.

(3) Before the peak strength, fractures first appear at both ends of the flaw, followed by the type-II fractures beginning to generate at the top and bottom of the cavity. At the moment of the peak strength, the type-II fractures between the ends of the flaw and the side wall of the cavity run through completely. After the peak strength, the type-II fractures between the

cavity and the boundary of the specimen begin to expand and gradually run through.

Data Availability

The data used to support the findings of this study are included within the article. The stress-strain curve and AE count used for analyzing experimental and calculative results are archived from the EXPCAL database at https://figshare.com/s/f466092970b125f220e0.

Conflicts of Interest

The authors declare that they have no conflicts of interest.

Acknowledgments

References

[1] R. H. C. Wong, C. A. Tang, K. T. Chau, and P. Lin, "Splitting failure in brittle rocks containing pre-existing flaws under uniaxial compression," *Engineering Fracture Mechanics*, vol. 69, no. 17, pp. 1853–1871, 2002.

[2] S.-Q. Yang, H.-W. Jing, and T. Xu, "Mechanical behavior and failure analysis of brittle sandstone specimens containing combined flaws under uniaxial compression," *Journal of Central South University*, vol. 21, no. 5, pp. 2059–2073, 2014.

[3] L. N. Y. Wong and H. H. Einstein, "Crack coalescence in molded gypsum and carrara marble: part 1. Macroscopic observations and interpretation," *Rock Mechanics and Rock Engineering*, vol. 42, no. 3, pp. 475–511, 2009.

[4] L. N. Y. Wong and H. H. Einstein, "Crack coalescence in molded gypsum and carrara marble: part 2-microscopic observations and interpretation," *Rock Mechanics and Rock Engineering*, vol. 42, no. 3, pp. 513–545, 2009.

[5] S. Q. Yang, D. S. Yang, H. W. Jing, Y. H. Li, and S. Y. Wang, "An experimental study of the fracture coalescence behaviour of brittle sandstone specimens containing three fissures," *Rock Mechanics and Rock Engineering*, vol. 45, no. 4, pp. 563–582, 2012.

[6] S.-Q. Yang, Y.-H. Huang, H.-W. Jing, and X.-R. Liu, "Discrete element modeling on fracture coalescence behavior of red sandstone containing two unparallel fissures under uniaxial compression," *Engineering Geology*, vol. 178, pp. 28–48, 2014.

[7] M. Prudencio and M. Van Sint Jan, "Strength and failure modes of rock mass models with non-persistent joints," *International Journal of Rock Mechanics and Mining Sciences*, vol. 44, no. 6, pp. 890–902, 2007.

[8] H. Cheng, X. Zhou, J. Zhu, and Q. Qian, "The effects of crack openings on crack initiation, propagation and coalescence behavior in rock-like materials under uniaxial compression," *Rock Mechanics and Rock Engineering*, vol. 49, no. 9, pp. 3481–3494, 2016.

[9] R. P. Young, J. F. Hazzard, and W. S. Pettitt, "Seismic and micromechanical studies of rock fracture," *Geophysical Research Letters*, vol. 27, no. 12, pp. 1767–1770, 2000.

[10] B. D. Thompson, R. P. Young, and D. A. Lockner, "Fracture in westerly granite under AE feedback and constant strain rate loading: nucleation, quasi-static propagation, and the transition to unstable fracture propagation," *Pure and Applied Geophysics*, vol. 163, no. 5-6, pp. 995–1019, 2006.

[11] I. L. Meglis, T. M. Chows, and R. P. Young, "Progressive microcrack development in tests in Lac du Bonnet granite-I. Acoustic emission source location and velocity measurements," *International Journal of Rock Mechanics and Mining Sciences and Geomechanics Abstracts*, vol. 32, no. 8, pp. 741–750, 1995.

[12] X.-D. Zhao, H.-X. Zhang, and W.-C. Zhu, "Fracture evolution around pre-existing cylindrical cavities in brittle rocks under uniaxial compression," *Transactions of Nonferrous Metals Society of China*, vol. 24, no. 3, pp. 806–815, 2014.

[13] H. P. Xie, J. F. Liu, Y. Ju, J. Li, and L. Z. Xie, "Fractal property of spatial distribution of acoustic emissions during the failure process of bedded rock salt," *International Journal of Rock Mechanics and Mining Sciences*, vol. 48, no. 8, pp. 1344–1351, 2011.

[14] Y. Wang, X. Li, Y. F. Wu, C. Lin, and B. Zhang, "Experimental study on meso-damage cracking characteristics of RSA by CT test," *Environmental Earth Sciences*, vol. 73, no. 9, pp. 5545–5558, 2015.

[15] Y. Wang, X. Li, B. Zhang, and Y. Wu, "Meso-damage cracking characteristics analysis for rock and soil aggregate with CT test," *Science China Technological Sciences*, vol. 57, no. 7, pp. 1361–1371, 2014.

[16] X. P. Zhang and L. N. Y. Wong, "Cracking processes in rock-like material containing a single flaw under uniaxial compression: a numerical study based on parallel bonded-particle model approach," *Rock Mechanics and Rock Engineering*, vol. 45, pp. 711–737, 2012.

[17] X.-P. Zhang and L. N. Y. Wong, "Loading rate effects on cracking behavior of flaw-contained specimens under uniaxial compression," *International Journal of Fracture*, vol. 180, no. 1, pp. 93–110, 2013.

[18] X.-P. Zhang, Q. Liu, S. Wu, and X. Tang, "Crack coalescence between two non-parallel flaws in rock-like material under uniaxial compression," *Engineering Geology*, vol. 199, pp. 74–90, 2015.

[19] Y. Zhou, S.-c. WU, Y.-t. GAO, and A. Misra, "Macro and meso analysis of jointed rock mass triaxial compression test by using equivalent rock mass (ERM) technique," *Journal of Central South University*, vol. 21, no. 3, pp. 1125–1135, 2014.

[20] H. Lee and S. Lee, "An experimental and numerical study of fracture coalescence in pre-cracked specimens under uniaxial compression," *International Journal of Solids and Structures*, vol. 48, no. 6, pp. 979–999, 2011.

[21] Y. Zhou, G. Zhang, S. C. Wu, and L. Zhang, "The effect of flaw on rock mechanical properties under the Brazilian test," *Kuwait Journal of Science*, vol. 45, no. 2, pp. 94–103, 2018.

[22] J. X. Zhou, Y. Zhou, and Y. T. Gao, "Effect mechanism of fractures on the mechanics characteristics of jointed rock mass under compression," *Arabian Journal for Science and Engineering*, vol. 43, no. 7, pp. 3659–3671, 2018.

[23] Y. Zhou, J. F. Chai, and G. Han, "Meso numerical study on the failure mechanism of rock slope with bedding intermittent joints," *Engineering Review*, vol. 37, no. 3, pp. 272–280, 2017.

[24] D. O. Potyondy and P. A. Cundall, "A bonded-particle model for rock," *International Journal of Rock Mechanics and Mining Sciences*, vol. 41, no. 8, pp. 1329–1364, 2004.

[25] D. O. Potyondy, "A grain-based model for rock: approaching the true microstructure," in *Proceedings of Bergmekanikk i Norden 2010—Rock Mechanics in the Nordic Countries 2010*, pp. 225–234, Kongsberg, Norway, June 2010.

[26] D. O. Potyondy, "A flat-jointed bonded-particle material for hard rock BT," in *Proceedings of 46th US Rock Mechanics/ Geomechanics Symposium*, pp. 24–27, American Rock Mechanics Association, Chicago, IL, USA, June 2012.

[27] A. Misra and V. Singh, "Nonlinear granular micromechanics model for multi-axial rate-dependent behavior," *International Journal of Solids and Structures*, vol. 51, no. 13, pp. 2272–2282, 2014.

[28] P. Poorsolhjouy and A. Misra, "Effect of intermediate principal stress and loading-path on failure of cementitious materials using granular micromechanics," *International Journal of Solids and Structures*, vol. 108, pp. 139–152, 2017.

[29] P. A. Cundall and O. D. L. Strack, "A discrete numerical model for granular assemblies," *Géotechnique*, vol. 29, no. 1, pp. 47–65, 1979.

[30] N. Cho, C. D. Martin, and D. C. Sego, "A clumped particle model for rock," *International Journal of Rock Mechanics and Mining Sciences*, vol. 44, no. 7, pp. 997–1010, 2007.

The Scientific World Journal

Journal of
Applied Chemistry

Journal of
Nanomaterials

Scientifica

International Journal of
Polymer Science

Advances in
Chemistry

Advances in
Physical Chemistry

International Journal of
Analytical Chemistry

Hindawi

Submit your manuscripts at
www.hindawi.com

Advances in
Condensed Matter Physics

Journal of
Chemistry

International Journal of
Biomaterials

Advances in
High Energy Physics

Journal of
Engineering

Journal of
Nanotechnology

International Journal of
Corrosion

Journal of
Materials

BioMed
Research International

Advances in
Tribology

Advances in
Materials Science and Engineering